AD A098874

DTIC FILE COPY

OFFICE OF NAVAL RESEARCH

Contract N00014-79-0622

Task No. NR 056-729

TECHNICAL REPORT NO. 2

Gasdynamics of Very Small Laval Nozzles

by

O. Abraham, J. H. Binn, B. G. DeBoer and G. D. Stein

Prepared for Publication

in

Physics of Fluids

Northwestern University
Departments of Mechanical and Nuclear Engineering
Chemistry, and Physics
Evanston, Illinois 60201

April, 1981

SECURITY CLASSIFICATION OF THIS PAGE (When Data Entered)

REPORT DOCUMENTATION PAGE		READ INSTRUCTIONS BEFORE COMPLETING FORM
1. REPORT NUMBER: Technical Report	2. GOVT ACCESSION NO. AD-A098 874	3. RECIPIENT'S CATALOG NUMBER
4. TITLE (and Subtitle): Gasdynamics of Very Small Laval Nozzles		5. TYPE OF REPORT & PERIOD COVERED: Interim
		6. PERFORMING ORG. REPORT NUMBER
7. AUTHOR(s): O. Abraham, J. H. Binn, B. G. DeBoer and ~~G. D. Stein~~ Gilbert D. Stein		8. CONTRACT OR GRANT NUMBER(s): N00014-79-C-0622
9. PERFORMING ORGANIZATION NAME AND ADDRESS: Northwestern University, Departments of Mechanical and Nuclear Engineering, Chemistry, and Physics Evanston, Illinois 60201		10. PROGRAM ELEMENT, PROJECT, TASK AREA & WORK UNIT NUMBERS: NR 056-729
11. CONTROLLING OFFICE NAME AND ADDRESS: Office of Naval Research Chemistry Program Code 472 Arlington, Virginia 22217		12. REPORT DATE: April 1981
		13. NUMBER OF PAGES: 45
14. MONITORING AGENCY NAME & ADDRESS (if different from Controlling Office): ONR, Chicago 536 S. Clark Street Chicago, Illinois 60605	(12) 24	15. SECURITY CLASS. (of this report): Unclassified
		15a. DECLASSIFICATION/DOWNGRADING SCHEDULE

16. DISTRIBUTION STATEMENT (of this Report)

Distribution of this document has been approved for public release and sale; its distribution is unlimited.

(14) TR-2

17. DISTRIBUTION STATEMENT (of the abstract entered in Block 20, if different from Report)

(15) N00014-77-C-0622

18. SUPPLEMENTARY NOTES

Prepared for publication in Physics of Fluids, June, 1981.

19. KEY WORDS (Continue on reverse side if necessary and identify by block number)

Clusters, Nucleation, Laval nozzles, Gasdynamics, Rayleigh scattering, SF_6, Ar

20. ABSTRACT (Continue on reverse side if necessary and identify by block number)

An investigation of diverging supersonic nozzles with throat diameters in the range of 0.025 to 0.25 mm has been carried out using gasdynamic measurements for a variety of gases and mixtures with sulfur hexafluoride. Due to the small nozzle size, boundary layers, although thin, may consitute a major fraction of the flow or, indeed at low pressures, may be fully developed. Nevertheless these nozzles have been shown to be very efficient for production of clusters condensed from the expanding gas. They produce orders of magnitude increases in molecular beam intensities, relative to

DD FORM 1473, 1 JAN 73 EDITION OF 1 NOV 65 IS OBSOLETE
S/N 0102-014-6601

SECURITY CLASSIFICATION OF THIS PAGE (When Data Entered)

(9) (6) (10) (11) (12)

145760

81 5 12 035

SECURITY CLASSIFICATION OF THIS PAGE(When Data Entered)

20. the conventional, "isentropic" free jet sources. The effects of gas properties and nozzle design on performance have been analyzed and compared to theoretical solutions to the governing equations of motion including cluster nucleation and growth.

SECURITY CLASSIFICATION OF THIS PAGE(When Data Entered)

GASDYNAMICS OF VERY SMALL LAVAL NOZZLES

Oommen Abraham, Jack H. Binn,[a] Barry G. DeBoer,[b] and Gilbert D. Stein
Northwestern University
Gasdynamics Laboratory
Evanston, Illinois 60201

ABSTRACT

An investigation of diverging supersonic nozzles with throat diameters in the range of 0.025 to 0.25 mm has been carried out using gasdynamic measurements for a variety of gases and mixtures with sulfur hexafluoride. Due to the small nozzle size, boundary layers, although thin, may constitute a major fraction of the flow or, indeed at low pressures, may be fully developed. Nevertheless these nozzles have been shown to be very efficient for production of clusters condensed from the expanding gas. They produce orders of magnitude increases in molecular beam intensities, relative to the conventional, "isentropic" free jet sources. The effects of gas properties and nozzle design on performance have been analyzed and compared to theoretical solutions to the governing equations of motion including cluster nucleation and growth.

PACS Numbers

1.) 47.55.Ea
2.) 47.55.kf
3.) 82.60.Nh
4.) 36.90.+f

a) Present address Midwesco Corp., Chicago, Illinois 60648
b) Present address GTE Sylvania Laboratory, Salem, Massachusetts 01970

INTRODUCTION

The study of small Laval nozzles has been undertaken in our laboratory as part of a research investigation into the properties of microscopic atomic or molecular particles. These nozzles constitute the source or first stage of a molecular beam apparatus which will provide a continuous stream of clusters in a high vacuum environment. It is well known that when a gas supersaturates in an adiabatic expansion the amount of undercooling that occurs before the onset of condensation depends on the cooling rate in the expansion. The slower the expansion, the smaller the amount of undercooling for cases where the expansion is continuum or collision dominated. For supersonic expansions the cooling rate scales with the throat dimension. Thus, larger nozzles will form droplets earlier in the expansion (i.e., at lower supersaturations and higher temperatures) than for small nozzles. Free jet or uncontrolled expansions into a high vacuum environment represent the most rapid, in fact the upper limit, cooling rate attainable in an adiabatic gas expansion. Thus, it is expected that a free jet expansion will produce far less condensate than a controlled Laval nozzle expansion of the same size. This is in fact the case as has been demonstrated previously.[1-5]

The use of small nozzles has become attractive for a number of important technological applications. One method of uranium isotope separation involves the adiabatic cooling of UF_6 to as cold a temperature as possible for use of tunable spectroscopic selection of isotopes.[6,7] Therefore, small nozzles are potentially useful in that they delay nucleation due to their rapid cooling rates and yet maintain relatively high cluster densities compared /with the uncontrolled free jet expansions. Another application which is being implemented in Germany involves a small Laval nozzle expansion to produce clusters of hydrogen to be used for fusion machine fueling and heating.[8,9] A prototype of this scheme is currently under

evaluation. A third use for these small nozzles in conjunction with a high vacuum, molecular beam type of configuration, would be to form small metal or semiconductor clusters for production of thin film devices.[10] The prospect of producing thin films with unusual or more uniform properties is the goal here. Finally, there are a number of applications for small nozzles in basic research. Primarily, they can be used as an efficient source of small clusters in order to study the physical properties of the clusters themselves or to use them in the study of atoms or molecules adsorbed onto them.

It is perhaps ironic that the development of molecular beam sources has gone through a couple of full circles. The initial sources in the 1930's were orifice or free jet expansions but at such low pressures that they were effusive in nature. Then, in 1951 it was suggested that the source pressure be increased and that the orifice be replaced with a hypersonic nozzle to make use of the so-called Mach focusing in order to increase beam intensity.[11,12] Due to some problems with regard to viscous effects and flow blockage, in the particular configuration considered, this technique was dropped in favor of high pressure free jet expansions which eliminated the viscous effects but retained the advantages of Mach focusing. This method has been used up to the present time as a beam source for a great variety of basic and applied research.[13-15] Recently, with the advent of greatly increased interest in the study of small aggregates in the gas phase, the Laval nozzle has re-emerged as an important device. The design, however, is substantially different from that originally proposed.

As an example, consider the enormous increase in cluster beam intensity from a Laval nozzle as compared with a free jet source (with the same throat diameter). The relative beam intensity of a pure argon cluster beam is shown in Fig. 1. By the time the source pressure is raised to p_o = 3 Bar (1 Bar = 10^5Pa = Newton/m^2 = 0.987 atm = 750 Torr) the beam intensity is off scale for the ionization gage detector used in this experiment. On the other hand, even at p_o = 11 Bar the free jet beam intensity is so low that it was not usable for our electron beam diffraction experiments. Thus, it becomes obvious, both from theoretical considerations as well as experimental evidence, that the controlled expansion of a small Laval nozzle is far superior to that of the free jet with respect to making cluster beams.

That this great enhancement in beam intensity exists has been demonstrated in several laboratories.[1-4] However, in order to understand the dynamics of the expansion in some detail, to be able to predict when condensation will begin for a given gas or gas mixture, and to determine how to design nozzles for future applications, a series of gasdynamic studies has been undertaken. For example, it is known that solid boundaries will grow boundary layers which for normal flow situations would be thin at these pressures. However, even thin boundary layers (of the order of 0.1 mm) can constitute a significant fraction of the nozzle radius or even the entire radius (i.e., fully developed flow). Nevertheless, even though there are viscous effects in small nozzles, there are conditions in which the clustering is still far superior to the "inviscid" free jet expansions. How important and under what flow conditions are viscous effects important or dominant in the small nozzle expansions? Is there an isentropic core in these expansions and if so under what circumstances? Is it possible to design nozzles which use helium as a coolant or carrier gas when the viscous effects in helium flows are much greater than for heavier species, that is, species with much greater collision cross sections? Is it possible to optimize the design parameters such as throat size, divergence angle, nozzle length and contour to produce clusters of given concentrations and/or size? Since pumping capacity in high vacuum systems is always a problem, how small a nozzle can one use and still get sufficient beam densities?

EXPERIMENTAL CONFIGURATION

The apparatus built to test nozzles is shown in Fig. 2. It is connected to the laboratory foreline manifold which is pumped by two mechanical pumps in series with a large enough capacity so that the pressure downstream of the nozzle exit, p_A, is in the range of 0.01-0.1 Torr. The nozzles are axisymmetric and made from glass capillary tubing with entrance diameters D_o = 0.025-0.3 mm with exit diameters D_e = 3-4 mm. Several different nozzle extensions are used to test the effect of nozzle length on performance. A static pressure tap is installed in these extensions in order to avoid drilling holes in the glass. The static pressure at the nozzle exit, p_1, is measured using a 10 Torr capacitance manometer.

Stagnation chamber pressure p_o and temperature T_o are also measured. Gas is supplied from bottles either as pure vapor or as mixtures of known mole fraction. Downstream of the nozzle exit a Pitot tube is mounted on a pressure transducer and manipulated with x-y-z motion capability. Thus, the total pressure, p_{02}, can be measured as a function of position either along the direction of flow or normal to it. T_o is always near room temperature and p_o is varied from 1 to 11 Bar. Since it is known from the molecular beam experiments that condensation will occur in these nozzles as p_o is increased, an argon ion laser and associated optics are included in order to detect the onset of nucleation just beyond the exit of the nozzle.

Results from four nozzles will be discussed in this paper and their contours are shown in Fig. 3. The diameter has been expanded by a factor of 8 to highlight the differences. Nozzle 7 looks like a cut-off version of Nozzle 4 with respect to the downstream contour but has a larger throat diameter. Nozzle 1 has the lowest divergence angle near the throat, θ_T, and Nozzle 6 the greatest. Nozzle 1 opens up more rapidly than the others toward the exit. Nozzle 7 has the smallest exit diameter, 2 mm, and Nozzle 6 is the shortest. In order to get an idea of the actual contour Nozzle 7 is also plotted on a 1:1 scale showing that the expansion is indeed very gentle. Two angles are used to characterize each nozzle defined as:

$$\theta_T = \tan^{-1}\left(\frac{dD}{dx}\right)_{x=o}, \qquad (1)$$

$$\theta_N = \tan^{-1}\left(\frac{D_e - D_o}{L}\right), \qquad (2)$$

where L is nozzle length.

Note that none of these nozzles has a converging section. This is done mainly to eliminate boundary layer growth through the minimum section (throat) of the nozzle. Also, since they have relatively high exit Mach numbers, conditions at the entrance up to Mach 1 will not significantly influence conditions at the exit. Three different exit configurations are shown in Fig. 3. They have the effect of reducing nozzle length going from A to C, with the additional length being 5 mm, 0.5 mm, and 0. The geometrical contours of the nozzles are measured using precision drill rods as plug gages. These data are used in a computer program to provide a best fit using a seventh-order polynomial

$$D(x) = \sum_{i=o}^{7} a_i x^i , \quad (3)$$

where the coefficient a_i and other pertinent dimensions for the nozzles are given in Table I.

MEASUREMENTS AND GASDYNAMIC INTERPRETATIONS

The basic experimental procedure is as follows:

(1) Install a particular nozzle and nozzle exit extension.
(2) Choose a particular gas mixture to be used for a complete set of measurements.
(3) Run at constant pressure, measure p_o, T_o, p_1, p_{02} on centerline.
(4) Record Pitot pressure traces as a function of x, y, or z.
(5) Take intermittent measurements of light scattering at nozzle exit.
(6) Change p_o and repeat 3-5 above.
(7) Change gas or gas mixture and repeat 2-6.
(8) Change nozzle and/or nozzle exit extension and repeat 2-7.

It would, of course, be desirable to have measurements along the complete nozzle contour, but this would have entailed an enormous design and instrumentation program. Also, since the primary interest is in the flow out of the nozzle exit, it is the properties at this point which are of greatest concern. The data are summarized in Table II.

The first level of analysis makes use of the listed measurements in conjunction with straightforward, one-dimensional gasdynamic analysis. The single most important parameter for characterizing flow conditions is the Mach number at the nozzle exit which is calculated in three ways. If one assumes that there is an isentropic core, then p_1 and p_o will yield a Mach number via the well known relation

$$\frac{p_1}{p_o} = \left(1 + \frac{\gamma - 1}{2} M_s^2\right)^{-\frac{\gamma}{\gamma - 1}} , \quad (4)$$

where γ is the ratio of specific heats and M_s is the Mach number at the exit using static pressure measurements. The second method of calculating an exit Mach number is to use the Pitot pressure measurement. Here, the flow must also be assumed to be isentropic (on the centerline) so that the total pressure ahead of the Pitot probe is the same as p_o. With this assumption the Mach number can be obtained with the supersonic Pitot equation:

$$\frac{p_o}{p_{02}} = \left(\frac{2\gamma M_p^2 - \gamma + 1}{\gamma + 1}\right)^{\frac{1}{\gamma - 1}} \left(\frac{2 + (\gamma - 1) M_p^2}{(\gamma + 1) M_p^2}\right)^{\frac{\gamma}{\gamma - 1}} . \quad (5)$$

The third method for calculating exit Mach number is to make use of the so-called Pitot-Rayleigh equation. This requires only local measurements, that is, the static pressure at the exit p_1 and the centerline Pitot pressure p_{02} at the same location in the nozzle as the static pressure tap. This method does not rely on any previous history of the centerline flow, that is, it does not have to be isentropic. Since the nozzle angular gradients are very small, treating the flow as one dimensional is a good assumption and thus p_1 is also the centerline static pressure. The Pitot-Rayleigh Mach number M_R is obtained using

$$\frac{p_1}{p_{02}} = \left(\frac{2\gamma M_R^2 - \gamma + 1}{\gamma + 1}\right)^{\frac{1}{\gamma - 1}} \left(\frac{2}{(\gamma + 1) M_R^2}\right)^{\frac{1}{\gamma - 1}} . \quad (6)$$

The exit Mach numbers calculated in the three ways described here are shown plotted in Fig. 4 for Nozzle 7 as a function of p_o for argon expansions. Results for the long nozzle extension A are shown as the dotted curves and the short nozzle extension B as solid lines. First of all, note that both M_s and M_p are greater than the Pitot-Rayleigh Mach number M_R. This is a reflection of the fact that the centerline or core flow is not isentropic. When comparing the results of the long and short nozzle extensions, we see that the static Mach numbers agree but the Pitot and the Pitot-Rayleigh do not. If it is assumed that the additional nozzle length results in increased viscous dissipation, then the larger values for M_p and the smaller values of M_R are qualitatively consistent. It is interesting that the static Mach number M_s is the same in both cases. In Fig. 4 (b) we see the results using the same nozzle for sulphur hexafluoride, SF_6. Here, the Mach numbers computed in all three ways are in fairly close agreement. This can be interpreted to mean that there is relatively little viscous dissipation on the centerline or core flow, i.e., that the core flow is isentropic.

It is also noteworthy to point out that all of the Mach number curves are nearly flat beyond p_o = 3 Bar. This is normally interpreted to mean that the boundary layers in the nozzle are not changing with increasing pressure and thus that there is indeed an isentropic core with size not

varying appreciably with pressure. However, since the three Mach numbers do not agree, except in the case of SF_6, there must have been some entropy production between the stagnation chamber and the nozzle exit. Beyond $p_o = 3$ Bar there is some entropy increase in the flow due to latent heat release due to condensation, except in the case of pure SF_6 and He. The discrepancy between the Mach number based on the geometric area ratio, M_G and the other Mach numbers is due, of course, to the boundary layer.

In order to obtain a more complete picture of the nozzle flow, Pitot traverses perpendicular and parallel to the flow direction are taken. Pitot traverses across the flow just beyond the nozzle exit (i.e. along the y direction with $x = 0$, see Fig. 3) are shown in Fig. 5 for two of the nozzles fitted with the long nozzle extension A. The Pitot tube has an o.d. of 0.5 mm and an i.d. of 0.25 mm and is set 0.76 mm from the nozzle exit. Figure 5(a) shows the results for both helium and argon expanded through Nozzle 6. The first thing to be noticed is that wherever there are flat sections of the profile, they constitute relatively small fractions of the exit diameter. For argon, the first evidence for a flat part of the Pitot (and therefore the velocity) profile appears at $p_o = 2.5$ Bar. The helium on the other hand must be expanded from a stagnation pressure of nearly 8 Bar before a level part of the Pitot trace is seen. The level section is interpreted as a flat velocity profile, i.e., a region outside the boundary layer. It is also seen that the flat velocity profile disappears for argon at higher pressures. This is believed due to the massive condensation occurring at these pressures and the possibility that the droplets are large enough to traverse the stand-off shock wave and enter the probe before complete evaporation.

The Pitot traverse measurements at the exit for Nozzle 4 are shown in Fig. 5(b). The most important difference between Nozzle 4 and the others is that its throat diameter is smaller by a factor of 2 or more. Thus, viscous effects can reach the centerline from the wall more readily. Here, it is seen that even starting pressures as high as 10 Bar produce no flat profile. Also notice that the magnitude of the Pitot pressure is around 5 Torr as compared with 120 Torr in Nozzle 6, an enormous difference. Even the argon must be expanded up to nearly 8 Bar before a flat velocity profile is obtained. Recall that the downstream ambient pressure, p_a in Fig. 2, is in the range of 0.1-0.01 Torr and so there is an additional expansion beyond the nozzle exit. Also, as the free jet continues downstream of the nozzle exit, there will be a mixing zone with the ambient gas.

Pitot traces along the nozzle centerline show a variation in pressure with x at the lower pressures for argon and at all pressures for helium. In Fig. 6 Pitot profiles are shown at several x locations from the

exit of the nozzle downstream. The flow is argon through Nozzle 1, exit configuration B [i.e., Nozzle 1(B)] with the exit defined as 0.5 mm beyond the end of the glass nozzle (see Fig. 3). Many of the Pitot profiles with this configuration show pressure bumps or "horns" on either side of the centerline. This type of feature has been observed in supersonic boundary layer flow as the Pitot probe approaches the solid boundary.[16] Under these circumstances the shock wave standing off the Pitot probe can interact with the boundary layer causing separation upstream of the probe thus changing the flow field seen by the Pitot tube. This explanation is consistent with all of the Pitot traverses that we have made in the course of these studies. The horns have been seen only when the probe is within the nozzle or in the neighborhood of the exit, i.e., close to solid boundaries. It also disappears in nozzle flows where $p_o \leq 3$ Bar. As the probe moves out of the nozzle the horns get smaller and then disappear by the time the probe is 1.5 mm downstream (i.e., $x/D_e = 0.6$). Notice also that the centerline Pitot pressure is dropping as the probe is moved farther downstream.

The symmetry of the horns is related to the direction the probe is moving, that is, away from or toward the solid boundary. When the probe direction is reversed, the asymmetry of the Pitot profile is reversed. The Pitot profiles are not taken as continuous traverses across the flow, but as discrete points waiting a sufficient time at each point to insure that no time lag appears in the measurements.

An extensive set of Pitot profiles has been taken for a great variety of flows in several of the nozzles. An example is provided in Fig. 7 for Ar and Ar-SF_6 mixtures in Nozzle 7-B. The Pitot probe is located 0.5 mm into the nozzle, at the plane between the glass nozzle and the exit extension (see Fig. 2 or 3). The effect of the SF_6 on the boundary layer growth can be seen. At $p_o = 3$ Bar the flat portion of the profile is quite small in Ar flow and gets larger as the percentage of SF_6 is increased. Thus, SF_6 reduces the boundary layer thickness. (Although the flows presented here were all steady, under some circumstances, especially with high SF_6 mole fractions, the flow became unsteady when probed by the Pitot tube.) As expected, the increase in the size of the core flow with starting pressures is evidenced in all three sets of data.

Because the Pitot probes must be smaller than the characteristic flow diameter and since the density in the flow near the exit is falling rapidly,

there is some concern as to whether there might be significant corrections to the one-dimensional Pitot probe theory assumed for Eqs. (5) and (6).

It is known that due to viscous effects Pitot tube measurements in the flow field will be different from that of the true total pressure if the Reynolds number of the probe Re_p is less than 100 [17] (based on probe diameter and properties just ahead of the probe but behind the detached shockwave). In the range $100 > Re_p > 10$ the measured value falls to about 85% of the theoretical value and then rises above the theory for $Re_p < 10$. In order to test this effect it is necessary to probe a flow of known properties. The obvious choice for this investigation is the use of free jet orifices. The theory for free jet expansions has been verified many times and with a variety of different types of measurement.[18] Pitot data have been taken with two different orifices by different investigators more than a year apart. They are converted to Mach number using Eq. (5) and compared in Fig. 8 to the theoretical Mach number given by Ashkenas and Sherman:[19]

$$M = A\left(\frac{x-x_o}{D}\right)^{\gamma-1} - \frac{1}{2}\left(\frac{\gamma+1}{\gamma-1}\right)\Big/\left[A\left(\frac{x-x_o}{D}\right)^{\gamma-1}\right], \qquad (7)$$

where A and x_o/D are constants dependent on γ with the following values: for $\gamma = 5/3$, $A = 3.26$, $x_o/D = 0.075$; for $\gamma = 1.4$, $A = 3.65$, $x_o/D = 0.40$. The earlier data are from an orifice with throat size 0.155 mm for argon, helium and nitrogen while the later data are for argon only using an orifice of 0.65 mm diam. The error bars on the earlier data are due to an uncertainty in the probe location with regard to the exit of the orifice. It is seen however, that the data fit the theory quite well, but are slightly lower than the theory except for the helium data without error bars (i.e., large orifice experiments). This small deviation may be due to condensation effects. All data presented in Fig. 8 are for high enough starting pressures p_o so that $Re_p > 100$, i.e., no pressure corrections are required. At lower p_o the deviation between measurements and theory can be reconciled with the Pitot correction.[17] Thus, the Pitot-Reyleigh equation (6) can be used with confidence if $Re_p > 100$ and all of the results presented in this paper meet this criterion.

The exit Mach number has been determined for numerous gases and nozzles. The two most important factors affecting the value of the Mach number are dynamic viscosity μ and specific heat ratio γ. Increasing μ and decreasing γ will lower the Mach number. Also as p_o is increased, latent heat due to condensation will decrease the Mach number slightly. The results for Nozzle 7 are presented in Fig. 9(a) and show a Mach number plateau with increasing pressure for Ar, Ar-SF_6 mixtures, and SF_6. At the higher pressures the Mach number for Ar, 3 and 6% SF_6-Ar mixtures all occur at a value of about 5.5. Thus, in this range the counteracting effects of decreasing γ and decreasing viscosity with increasing SF_6 mole fraction, plus the effect of heat addition just cancel out. The pure SF_6 would be shifted to a much lower Mach number

on the basis of γ reduction only, but the reduced viscous effects in these flows result in a thinner boundary layer thus raising the Mach number. The net result is a decrease in Mach number to about 5.0. The 12.5% SF_6-Ar appears to be dominated more by the γ and heat addition than by the effects of lower viscosity, resulting in an exit Mach number of 4. The increased viscous effects in the helium flows are evident by their much reduced Mach numbers in spite of the fact that helium has a high γ. Neither the He nor the 12% SF_6-He mixture reaches a plateau.

Now consider the results of Nozzle 1 relative to Nozzle 7. Careful inspection of the contours in Fig. 3 reveal that Nozzle 1 has a slower area expansion near the throat but a more rapid increase in the latter part. Thus small changes in viscous effects between Ar and the 3 and 6% Ar-SF_6 mixtures produce larger differences in Nozzle 1 due to the slower opening throat area. This results in higher exit Mach numbers with increased mole fraction of SF_6 up to 6% [see Fig. 9(b)]. However, the helium mixtures perform consistently better in Nozzle 1. The small section near the throat is about as detrimental as it is in Nozzle 7; however, the downstream section with a more rapid opening will reduce the viscous dissipation in this region. The viscous effects in the argon expansions are minimal in this section for both nozzles. The 12.5% SF_6-He mixture reaches a Mach number plateau above 4 Bar. Thus, the data provide some indication of what nozzle features influence gas expansions with different viscous effects (i.e., Reynolds number $Re = \rho u D/\mu$ where ρ is density) and specific heat ratios.

In addition to the Mach number, other dimensionless parameters are calculated. The Reynolds number is used to characterize viscous effects, the Knudsen number (and its inverse Kn^{-1}) is an indication if and when rarefied gasdynamics is of importance, and the Prandtl number Pr indicates the relative importance of thermal to viscous boundary layers. The Prandtl number is $Pr = \mu c_p/k$ where c_p is the constant pressure specific heat and k is the thermal conductivity and does not vary greatly through the nozzle or with changes in p_o. Typical values for Ar are 0.65 to 0.7 and for SF_6 0.44 to 0.48. Representative values for Re and Kn^{-1} as a function of p_o for Nozzle 7(b) are shown in Fig. 10. Reynolds and Knudsen numbers ($Kn = \lambda/D$ where λ is the mean-free-path) range over two orders of magnitude. This is true for all SF_6-Ar, but He and SF_6-He have about an

order of magnitude greater variation. There is less than a factor of 2 change with pressure.

If relationships can be established for boundary layer effects, they could then be used to predict many of the nozzle characteristics without having to conduct gasdynamic experiments. One such correlation is given in Fig. 11. The boundary layer thickness δ is estimated here using the Pitot pressure traverses across the exit of the nozzle. Core flow is taken as that part of the profile which is flat and the remainder is assumed to be boundary layer. The displacement thickness δ_d is estimated using M_R to get an isentropic area A_I and $A_G/A_I = r^2/(r-\delta_d)^2$. The results provide the magnitude of the boundary thickness, with $\delta > \delta_d$ as it should be, and $\delta = r$ (fully developed flow at the exit) for $Re < 4{,}000$.

Pitot and static pressure data for several nozzles and gases are converted to Mach number, M_R, and plotted in Fig. 12. The ratio M_R/M_G is related to the displacement thickness. When plotted as a function of $Re^{\frac{1}{2}}$ (related to laminar boundary layer growth) times Pr (ratio of thermal to viscous boundary layer thickness), the results fall along lines having a monotonic variation with kinematic viscosity, $\nu = \mu/\rho$.

COMPARISON TO SOLUTION OF GOVERNING EQUATIONS

A complete two-dimensional solution to the equations of motion including viscosity and heat conduction effects along with nucleation and growth of the condensed phase, with its attendant latent heat release, would constitute an enormous undertaking both in terms of man-years and computer funds. The authors feel this is not warranted in terms of the goals of this work which require an understanding primarily of the centerline flow. A one-dimensional approach, incorporating some of the two-dimensional features for momentum and energy transport, has been developed. This model includes all important physical phenomena for the flow process but requires that several features be characterized by empirical parameters. They are adjustable but must be chosen in a self-consistent and physically meaningful way. The particular approach chosen here is not unique in the sense that it is the only way to pursue a simplified description of this process. It can provide, however, some theoretical guidance and insight with modest use of computer time.

Detailed centerline computations for the case of 3% SF_6-Ar expansions have been carried out for Nozzle 7. One-dimensional steady state equations for conservation of mass, momentum and energy have been employed with an additional term for viscous effects in the momentum equation and a term for heat conductivity within the gas in the energy equation:

$$\rho A u = \dot{m} \qquad \text{(continuity)} \qquad (8)$$

$$dp + \rho u du = dP_\nu \qquad \text{(momentum)} \qquad (9)$$

$$d(h + \frac{u^2}{2}) = dq + dP_k \qquad \text{(energy)} \qquad (10)$$

where ρ is density, A is the nozzle cross-sectional area, u is velocity, $\dot{m}$ is the mass flow rate and is constant for steady flow, p is pressure, h is enthalpy, and q is the latent heat release per unit mass due to phase change, i.e., $dq = Ldg$ where L is the latent heat for the condensable (SF_6 here) and g is the mass condensed per mass of mixture (carrier gas, condensable vapor and condensate). The quantities dP_ν in the momentum equation (9) and dP_k in the energy equation (10) are "production" terms due to the transport of momentum (viscous effects) and energy (heat conduction) to the centerline flow. Density and enthalpy are for the mixture including the condensed phase if present, i.e., $\rho = \rho_i + \rho_v + \rho_k$ and $h = h_i + h_v + h_k = cp_i T + cp\, T + cT$. The subscript i is for the inert carrier gas (Ar or He), v is for the condensible vapor (SF_6), and k is for the condensed phase. The specific heat at constant pressure is c_p and c is the condensed phase specific heat. The perfect gas equation of state is

$$p = (1-g)\rho RT/\mathcal{M}_g \qquad (11)$$

where T is temperature and $\mathcal{M}_g$ is the molecular weight of the gas mixture which changes as condensation begins due to vapor depletion thus $(1-g)\rho = \rho_g$.

The boundary conditions at the solid wall are the no slip velocity condition and no heat exchange, i.e., an adiabatic wall. However, due to temperature gradients in the boundary layer, energy transport occurs within the gas resulting in heat flow from the periphery inward. For those situations where the boundary layers grow together making a fully developed flow, the two transport terms are brought into use in the governing equations.

The term dP_ν in Eq. (9) is then

$$dP_\nu = \mu \frac{\partial^2 u}{\partial r^2} dx, \qquad (12)$$

[see Ref. 20 Eq. (2-24a)] and dP_k in Eq. (10) becomes

$$dP_k = k \frac{\partial^2 T}{\partial r^2} + \frac{\partial T}{\partial r}\frac{\partial k}{\partial r} + \mu u \frac{\partial^2 u}{\partial r^2} + \mu\left(\frac{\partial u}{\partial r}\right)^2 + u \frac{\partial u}{\partial r}\frac{\partial \mu}{\partial r} \qquad (13)$$

[see e.g. Ref. 20 Eq. (7-5)] where μ is the dynamic viscosity and k is the thermal conductivity.

Since only the centerline flow is of interest in molecular beam applications, solutions of the entire two dimensional flow field are not desired and would require a substantial computational effort. The viscous and heat conduction "production" terms of Eqs. (12) and (13) are essential, however, for a physically meaningful description of the centerline flow. An integral approach is used[16] in which the production term in each volume element $dV = 2\pi r dr\, dx$ is summed over the flow volume cross section slice between x and x + dx (see Fig. 3) and divided by the slice volume to give an average value (for either dP_ν or dP_k)

$$\overline{dP} = \int_0^{r_w} 2\pi r dP dr\, dx \left(\int^{r_w} 2\pi r dr\, dx\right). \qquad (14)$$

In order to evaluate Eq. (14) the functions $u=u(r)$, $T=T(r)$, $\mu=\mu(T)$, and $k=k(T)$ must be specified.

Data for the temperature dependence of the viscosity and the thermal conductivity of Ar[21] and SF_6[22] are fitted with linear functions. The velocity distribution is assumed to be parabolic, where fully developed, going from zero at the wall to a maximum at the centerline (subscript c)

$$u(x,r) = u_c(x)(1-r^2/r_w^2), \qquad (15)$$

where r_w is the radial distance to the wall. The temperature profile is also assumed to be parabolic rising from the value at the centerline $T_c(x)$ to an adiabatic wall temperature T_{aw}. The use of a temperature recovery factor of the form $r = (T_{aw}-T_c)/(T_o-T_c)$ is frequently used in viscous flow[19] where T_o is the stagnation temperature $\cong 295K$. For a Prandtl number near unity (0.7) $r \cong 0.86$ giving $T_{aw} = 0.14\, T_c(x) + 25G$. The temperature distribution then becomes

$$T(x,r) = T_c(x) + \Delta T(r^2/r_w^2), \qquad (16)$$

where $\Delta T = T_{aw}-T_c$.

The average value of the transport or "production" terms, Eq. (14), for viscosity and heat conduction can now be evaluated and they are

$$\overline{dP}_\nu = \frac{-2u_c dx}{r_w^2}\left(\mu_c + \frac{3}{2}\frac{d\mu}{dT}\Delta T\right), \qquad (17)$$

and

$$\overline{dP}_k = \frac{dx}{\rho_c u_c}\left[\frac{2\Delta T}{r_w^2}\left(k_c + \frac{3}{2}\frac{dk}{dT}\Delta T\right) + \frac{u_c^2}{r_w^2}\left(\mu_c + \frac{d\mu}{dT}\frac{\Delta T}{3}\right)\right], \qquad (18)$$

where $d\mu/dT$ and dk/dT are obtained from the straight line curves fitted through the temperature dependent μ and k and averaged for the particular mole fraction of Ar and SF_6 at that x position.

Since the radial gradients dT/dr and du/dr are small near the flow centerline, the production terms dP_ν and dP_k in Eqs. (9) and (10) should be a small fraction, call it F_μ of the volume averaged term over all r. Thus, we can write

$$dP_\nu = F_\mu \overline{dP}_\nu,$$

and

$$dP_k = F_\mu \overline{dP}_k. \qquad (19)$$

The use of the integral technique eliminates the need for the actual velocity profiles so that $\overline{dP}_\nu(\overline{dP}_k)$ is not sensitive to the details of the velocity (temperature) distribution. Typical values of F_μ used to calculate the properties on the centerline are in the range 0.0001 to 0.0005. The point at which fully developed flow begins and ends can be varied in the program.

It should be stressed here that the radial distribution of properties are used only to compute the value of the production terms dP_ν and dP_k [Eqs. (17) and (18) substituted into Eq. (19)] which appear in Eqs. (9) and (10). The solution to the governing equations of motion, Eqs. (8), (9), and (10) are carried out with the use of an equation of state, Eq. (11), plus droplet nucleation and growth equations described by Eqs. (21) and (22). They are solved as a closed set of one-dimensional (x) flow equations with phase change and transport terms for viscosity and heat conduction. The boundary layer effects are handled in the usual way[22] with a displacement thickness which grows from zero thickness at the nozzle entrance to a value at the exit. δ_d, characterized by a non-dimensional thickness $\Delta = \delta_d/r_{we} = 2\delta_d/D_e$. The values for the centerline properties used in calculating dP_ν and dP_k are taken as those obtained from the one-dimensional solutions.

The variation of displacement thickness with x is provided for using an exponential growth equation giving the equivalent nozzle diameter as

$$D(x) = 2\left[r_w(x) - \delta_d(x_e)\left(\frac{x}{x_e}\right)^N\right], \qquad (20)$$

where x_e is the distance from nozzle entrance to exit and N was varied from 1 (i.e., linear) to 2.

In addition to the gasdynamic equations, the equations to describe droplet nucleation and growth are also included.[23-25] Due to the relatively high cooling rates for gases passing through these small nozzles, a correction to the steady state nucleation theory[26-32] is incorporated.[29] The steady state nucleation theory is applicable for nozzle cooling rates of up to 10^6 °C/sec. Cooling rates of 10^9 °C/sec, typical of free jet expansions, are thought to be too high to be dealt with using the nucleation rate theory. The nozzles in this paper have cooling rates in the range of 10^7-10^8 where adjustments to the steady state theory are expected to apply (corrections of a factor of 2-4 at most).

The steady state nucleation theory is a function of the thermodynamic variables obtained in conjunction with the solution to the governing equations (8)-(11),

$$J = \left(\frac{p_v}{kT}\right)^2 \left(\frac{2\sigma}{\pi m}\right) v_c \exp\left(-\Delta G^*/kT\right) , \qquad (21)$$

where J is the number of critical size (*) clusters formed cm^{-3} sec^{-1} and $\Delta G^* = 4\pi r^{*2}\sigma/3$ is the Gibbs free energy of formation of a critical size cluster, i.e., the size which is large enough to become a stable droplet of condensed SF_6. Here, p_v is the SF_6 vapor pressure, k is Boltzmann's constant, σ is the SF_6 surface tension, m is the mass of an SF_6 molecule, and v_c is the volume of one SF_6 molecule in the condensed phase. The critical radius is $r^* = 2\sigma v_c/kT \ln S$, where S is the SF_6 saturation ratio, $S=(p_v/p_{v\infty})_T$ with $p_{v\infty}$ the SF_6 vapor-liquid equilibrium pressure at temperature T.

Since the cluster size is small compared with the mean-free-path of the gas and since the condensate (SF_6) is a small fraction (3%) of the argon carrier gas, the droplet growth law is that obtained from elementary kinetic theory with a condensation coefficient α near 1.0. Thus, the growth law is

$$dO/dt = \alpha\beta O , \qquad (22)$$

where O is the droplet area $O=4\pi r^2$ and β is the SF_6 impingement rate per unit area, $\beta = p_v/(2\pi mkT)^{\frac{1}{2}}$. Taking proper account of the number of droplets formed at x, x+dx, plus the growth of previously nucleated clusters, the mass fraction condensed can be computed, $g=g(x)$, and since $dq=Ldg$ Eqs. (21) and (22) provide dq and g in Eqs. (3) and (4).

To summarize: Equation (19) provides the production or transport terms when boundary layer effects penetrate to the flow centerline, Eq. (20) provides the effective nozzle area A, Eqs. (21) and (22) provide dq and g, and $h=h(T)$. Therefore, Eqs. (8)-(11) can be considered, after the substitutions, as four equations in four unknowns, p, ρ, T and u. There are four adjustable parameters $x_\mu^\dagger$, Δ, N and F_μ. They are, respectively, the fraction of the centerline flow which suffers viscous dissipation, the fraction of the exit diameter which is displacement thickness [see Eq. (20)], the exponent for boundary layer growth [see Eq. (20)], and the fraction of the average viscous dissipation at any cross-section in the nozzle where the flow is fully developed [see Eq. (19)]. The method for determining these parameters will be discussed next.

The definition of $x_\mu^\dagger$ is given by $x_\mu^\dagger = (x_f - x_i)/L$ where x_i is the distance in which the boundary layer grows out to the centerline and x_f is the location downstream of x_i where velocity gradients normal to the flow are low enough that viscous effects are negligible. Thus the effects of the "production" terms dP_μ and dP_k in Eq. (19) are included in the flow from x_i to x_f. The calculations presented here are for Nozzle 7 only and x_i is taken as 3 mm. For $p_o \le 1$ Bar $x_f = L$, i.e., viscous effects occur along the entire nozzle length after x_i, giving a value of $x_\mu^\dagger = 0.88$ as seen in Table III. For SF_6 in Ar and $p_o > 1$ Bar the Pitot, and thus the velocity, profile is flat as seen in Fig. 7. However the stagnation pressure at the exit is less than p_o so there has been centerline viscous dissipation for some distances beyond x_i. Thus the viscous effects are again negligible before the flow exits the nozzle and therefore $x_f < L$. Although one expects x_f to vary with p_o, a single value was used for $p_o > 1$ Bar. The value chosen for x_f is chosen at a point in the nozzle where the slope of the contour begins to increase significantly, $x_f = 12.3$ mm, giving $x_\mu^\dagger = 0.37$ as seen in Table III. Thus $x_\mu^\dagger = 0.88$ for $p_o \le 1$ Bar and $= 0.37$ for $p_o > 1$ Bar.

The value of $\Delta \equiv 2\delta_d/D_e$ to be used in Eq. (20) for the effective area ratio is determined by matching the calculated exit Pitot pressure p_{02}, i.e., the value of the stagnation pressure at the exit, behind a normal shock, with the measured value, at a given p_o. The exponent governing the boundary layer growth in Eq. (20) is chosen such that the slope of the theoretical p_1 vs p_o curve is the same as the data for ± 1

Bar around the given value of p_o. The best fit was obtained using N=1.5 for all of the data analyzed for SF_6-Ar in Nozzle 7. The value of F_μ was determined by matching the exit static pressure p_1 for each initial pressure p_o.

Due to the high cooling rates in these nozzles, and densities typically falling to less than 1% of the starting density, vibrational relaxation for the SF_6 molecule is included using published relaxation times.[33] The program calculates all the thermodynamic variables, gasdynamic properties including velocity and Mach number, details of the phase change including nucleation rate, number of droplets formed, and size. The primary concern here is to match the gasdynamic properties, i.e., p_1 and p_{02}. These data for the 3% SF_6-Ar in Nozzle 7 are plotted as the circles in Fig. 13. As p_o is increased the boundary layer thickness δ, the displacement thickness δ_d, the centerline production dP_v and k, and the length of centerline viscous effects $x_\mu^\dagger$ may all change. The calculation procedure holds these parameters constant while p_o is varied and thus the theoretical results represent "planes" crossing the plane of the experimental data in a hyperspace.

Upon examining many sets of computer results using a systematic variation in parameters, a reasonable and consistent picture of the nozzle flow is obtained. The Pitot pressure data seen in Fig. 13(b) are shown intersected with lines of constant Δ. It is found that variation of N, F_μ and $x_\mu^\dagger$ all have virtually no effect on p_{02}. Thus Pitot pressure is determined once Δ is fixed for a given inlet p_o. The variation of Δ from 0.65 to 0.5 as p_o increases from 3 to 8 Bar, shown indirectly in Fig. 13(b) and explicitly in Fig. 14(c), is qualitatively correct since as the density increases the transport of momentum and energy from the nozzle wall is decreased giving thinner boundary layers. Below 3 Bar viscous effects (F_μ) have an important effect on the values of p_{02}.

Static pressure p_1 is much lower than p_{02} and changes in most of the listed parameters produce only small fractional changes in the static pressure. (The accuracy of the experimental data is ±0.02 Torr.) Variation of N in Eq. (20), results in a change of slope for p_1 vs p_o in Fig. 13(a). The best match to the slope of the data occurs for N=1.5 which was used for all the calculations presented here. The magnitude of p_1 for a given p_o is then determined by fixing F_μ.

The Pitot data below 2 Bar fall below the calculated values. This is believed to be due in part to a drop in measured Pitot pressure from that of the true Pitot pressure at low probe Reynolds numbers (i.e., less than 100) which are encountered in the flows at low p_o. Even when corrected the data fall below the curves for Δ=0.5-0.6. In this range the viscous effects are quite prevalent since boundary layers get thicker at lower Re and at 1 Bar an increase of F_μ to 0.0008 still does not match the Pitot data. An upper value for F_μ used here is set at that value which drives the Mach number subsonic.

In addition to the pressure results shown in Fig. 13 the results for Δ and M_G are summarized in Fig. 14. Displacement thickness Δ varies from 0.5 to 0.65. The exit Mach number levels off at 5.4. The computed results along with the parameters used are given in Table III. Since the program is run with discrete choices for parameters, the agreement with experimental measurement, although close, is not expected to be perfect in every case. The somewhat lower values of the theoretical Δ compared to $2\delta/D_e$ from measurement, is qualitatively correct since Δ is based on boundary layer displacement thickness while the measurements in Fig. 11 are velocity boundary layers and thus $\delta > \delta_d$ as expected.

DISCUSSION

Flows at higher pressures have thinner boundary layers, and smaller viscous dissipation occurring only in the early part of the expansion. The boundary layer becomes fully developed close to the nozzle entrance where the diameters and θ_T are very small. Further downstream where the nozzle angle opens up more rapidly, we assume that a boundary layer edge reappears, leaving a core flow with very little viscous dissipation, i.e., nearly isentropic but with a value of entropy greater than the starting value. This is consistent with the Pitot traverses normal to the flow at high pressures which have flat profiles near the center, indicating flat velocity profiles and thus little viscous effects in this region and with the fact that the stagnation pressure at the exit is less than p_o. As the pressure decreases the Reynolds number will decrease and the boundary layer increases. Thus, the point at which a boundary layer edge reforms will occur progressively further down the nozzle, resulting in a profile with a flat section that is a smaller

portion of the flow. For $p_o \geq 2$ Bar the flow remains fully developed along the entire nozzle except for a very short inlet region.

It should be emphasized that the amount of centerline dissipation seen in these flows appears relatively small, that is, in the range of 0.02-0.1% of the average dissipation at any given nozzle cross-section where the flow is fully developed. This picture is consistent with all of the gasdynamic data. However since the Geometric Mach Number, M_G, is much greater than the actual Mach Number, M_R, there are substantial boundary layers in the Nozzle [see Fig. 4(a)]. The viscous dissipation out to the centerline is also significant, i.e., no isentropic core, since M_R, M_p and M_s all differ by as much as 50 to 100%. (Recall that, even with a substantial amount of boundary layer, M_R, M_p and M_s should coincide if there is an isentropic core.) In addition, the droplet nucleation and growth calculations in this program predict condensation in agreement with both the measurement of laser light scattering and the ionization gage beam detection in the molecular beam configuration.[34] (There is experimental and theoretical evidence for condensation approaching 100% of the condensable species in the higher pressure runs.[3])

For some flow conditions, and especially with light carrier gases such as helium, viscous dissipation can be prevalent to such an extent that nozzles become less efficient than free jet expansions.[35] Nozzles have been designed so that nucleation of small mole fractions of noble gases in a helium carrier gas can be used for beam experiments.[35] In pure SF_6 expansions the boundary layers remain thin even in the very small entrance sections of several of the nozzles so that an isentropic core is maintained all the way to the exit.

The most important single parameter to characterize the properties of the flow that is produced by these nozzles is the exit Mach Number M_R. The Mach Number ratio M_R/M_G is found to correlate with $Pr_e Re_e^{0.5}$ and γ. The analysis of the data using one-dimensional gasdynamics, along with the calculation of thermodynamic properties and dimensionless quantities, has provided a means for designing small nozzle sources either to encourage or discourage condensation.

ACKNOWLEDGMENTS

The authors would like to thank Mr. Sang-Soo Kim for use of the argon

molecular beam results shown in Fig. 1 and Mr. Diancheng Chi for the large orifice data in Fig. 8. One of us (GDS) thanks Professor Alan L. Kistler for valuable suggestions and comments with respect to several aspects of both data and theoretical analysis. We are grateful to Mr. James F. Morris, the glassblower who made our nozzles, and Mr. Robert D. Klaub and his Machine Shop for construction of the remainder of the apparatus.

This research was supported in part by the Engineering Energetics section of the National Science Foundation and the Power Branch and the Chemistry Division of the Office of Naval Research.

REFERENCES

1. O. F. Hagena and W. G[illegible], J. Chem. Phys. 56, 1793 (1972)
2. O. F. Hagena, in Molecular Beams and Low Density Gas Dynamics, edited by P. P. Wegener (Marcel Dekker, New York, 1974), p. 93
3. S. S. Kim, B. G. DeBoer, and G. D. Stein, in Rarefied Gas Dynamics, edited by R. Campargue, (Commissariat a L'Energie Atomique, Paris, 1979), p. 1151
4. W. Obert, in Rarefied Gas Dynamics, edited by R. Campargue (Commissariat a L'Energie Atomique, Paris, 1979), p. 1181
5. B. J. C. Wu, P. P. Wegener, and G. D. Stein, J. Chem. Phys. 69, 1776 (1978)
6. B. J. C. Wu and G. A. Laguna, J. Chem. Phys. 71, 2991 (1979)
7. S. S. Fisher, Phys. Fluids 22, 1261 (1979)
8. E. W. Becker, H. Falter, O. F. Hagena, W. Henkes, R. Klingelhöfer, H. O. Moser, W. Obert, and I. Poth, Nucl. Fusion 17, 617 (1977)
9. E. W. Becker, H. Falter, O. F. Hagena, W. Henkes, R. Klingelhöfer, H. O. Moser, W. Obert, and I. Poth, in 1st Symposium on the Production and Neutralization of Negative Hydrogen Ions and Beams, edited by K. Prelec (BNL 50727 Brookhaven National Laboratories, Long Island, New York, 1977), p. 322.
10. T. Takagi, I. Yamada, K. Yanagawa, M. Kunori, and S. Kobiyama, J. Appl. Phys. Suppl. 2, Pt. 1, 427 (1974)
11. A. Kantrowitz and J. Grey, Rev. Sci. Instrum. 22, 328 (1951)
12. G. B. Kistiakowsky and W. P. Slichter, Rev. Sci. Instrum. 22, 333 (1951)
13. J. B. Anderson, in Molecular Beams and Low Density Gas Dynamics, edited by P. P. Wegener, (Marcel Dekker, New York, 1974), p. 1
14. R. E. Smalley, B. L. Ramakrishna, D. H. Levy, and L. Wharton, J. Chem. Phys., 61, 3463 (1974)

15. R. E. Smalley, L. Wharton, and D. H. Levy, in Accounts of Chemical Research, edited by J. Bunnett (American Chemical Society, Washington D.C., 1977). Vol. 10, p. 139
16. A. L. [illegible]atler (private communication)
17. J. L. Potter and A. B. Bailey, AIAA J. 2, 743 (1964)
18. J. B. Anderson, R. P. Andres, J. B. Fenn, and G. Maise, in Rarefied Gas Dynamics, edited by J. H. DeLeeuw (Academic, New York, 1966), Vol. 2, p. 106
19. [illegible] Ashkenas and F. S. Sherman, in Rarefied Gas Dynamics, edited by J. H. deLeeuw (Academic, New York, 1966), Vol. II, p. 84
20. F. M. White, Viscous Fluid Flow, (McGraw-Hill, New York, 1974), p. 576
21. The Matheson Unabridged Gas Data Book, Argon booklet, (Matheson Gas Products, East Rutherford, New Jersey, 1974), p. 4 and 7
22. The Matheson Unabridged Gas Data Book, Sulfur Hexafluoride booklet, (Matheson Gas Products, East Rutherford, New Jersey, 1974), p. 7 and 9
23. P. P. Wegener and A. A. Pouring, Phys. Fluids, 7, 352 (1964)
24. P. P. Wegener, Nonequilibrium Flows, edited by P. P. Wegener (Marcel Dekker, New York, 1969) Part I, p. 163
25. C. A. Moses and G. D. Stein, J. Fluids Eng., 100, 311 (1978)
26. A. Kantrowitz, J. Chem. Phys. 19, 1097 (1951)
27. R. F. Probstein, J. Chem. Phys. 19, 619 (1951)
28. H. Wakeshima, J. Chem. Phys. 22, 1614 (1954)
29. F. C. Collins, Z. Elektrochem. 59, 404 (1955)
30. R. P. Andres and M. Boudart, J. Chem. Phys. 42, 2057 (1965)
31. J. Feder, K. C. Russel, J. Lothe, and G. M. Pound, Adv. Phys. 15, 111 (1966)
32. F. F. Abraham, J. Chem. Phys. 51, 1632 (1969)
33. W. D. Breshears and L. S. Blair, J. Chem. Phys. 59, 5824 (1973)

34. O. Abraham, S. S. Kim, and G. D. Stein, (to be published)

35. S. S. Kim, D. C. Shi, and G. D. Stein, Proceedings of the Twelfth International Symposium on Rarefied Gas Dynamics, University of Virginia, (1980). Progress in Astronautics and Aeronautics, edited by S. S. Fisher (American Institute of Aeronautics and Astronautics, New York, 1981)

TABLE I
Nozzle Geometry

Nozzle Number	D_o cm	De cm	L cm	θ_T Deg	θ_N Deg	a_o	a_1	a_2	a_3	a_4	a_5	a_6	a_7
1	0.0137	0.256	3.05	1.78	4.61	0.0137	-0.6982	0.3843	-0.4834	0.3189	-0.0984	0.0113	0
4	0.0063	0.256	3.15	2.01	4.58	0.00635	-0.0248	0.1488	-0.2156	0.0450	-0.00637	0	0
6	0.0119	0.256	2.31	7.31	6.56	0.0119	0.1038	-0.0404	0.1133	-0.065	0.0102	0	0
7	0.0127	0.218	2.5	2.95	3.83	0.01277	-0.01553	0.1555	-0.18189	0.09671	-0.0058	-0.0092	0.0018

TABLE II
Gasdynamic Data

Nozzle	Gas	P_o Bar	P_1 Torr	P_{02} Torr	M_R
1	Ar	3	1.459	53.84	4.98
		4	1.663	60.65	4.95
		5	1.866	68.93	4.98
		6	2.067	75.40	4.95
		7	2.27	81.87	4.92
	0.125 SF_6 -He	3	2.13	20.78	2.69
		4	2.54	80.43	4.94
		5	2.92	93.37	4.96
	SF_6*	3	1.244	34.79	4.88
		4	1.562	43.06	4.84
		5	1.82	51.68	4.87
		6	2.121	58.87	4.86
		7	2.421	66.78	4.84
	0.125 SF_6 -Ar	2	1.31	23.65	3.71
		3	1.584	33.15	4.12
		4	1.866	45.93	4.35
		5	2.113	56.0	4.51
		6	2.303	63.18	4.60
		7	2.63	66.78	4.42
	0.03 SF_6 -Ar	2	1.236	36.99	4.58
		3	1.452	56.43	5.23
		4	1.743	68.53	5.26
		5	1.881	75.0	5.30
		6	2.107	82.47	5.25
		7	2.332	87.42	5.14
	0.0625 SF_6 -Ar	2	1.235	28.68	4.11
		3	1.487	51.68	5.04
		4	1.690	66.06	5.35

*Because γ for SF_6 is a function of temperature, the first iteration for M_R is obtained using $\gamma(T_o)$ which is then used to estimate exit temperature, T_e, and $\gamma(T_e)$ then used to get the final value of M_R.

TABLE II
Gasdynamic Data (Cont.)

Nozzle	Gas	P_o Bar	P_1 Torr	P_{02} Torr	M_R
		5	1.922	79.00	5.49
		6	2.174	87.62	5.44
		7			
		8	2.655	92.85	5.06
		9	2.898	102.0	5.08
	He	3	2.80	10.92	0.50
		4	3.18	29.11	2.43
		5	3.43	79.0	3.91
		6	3.62	158.6	5.42
		7	3.82	255.55	6.72
		8	4.03	352.09	7.69
4	Ar	2	0.485	1.37	1.25
		3	0.683	1.97	1.27
		4	0.870	2.66	1.32
		5	0.959	3.44	1.45
		6	1.008	7.12	2.12
		7	1.06	10.83	2.57
		8	1.11	15.60	3.03
		9	1.18	19.28	3.28
		10	1.24	22.93	3.50
	SF_6	4	0.575	4.82	2.68
		5	0.630	8.27	3.38
		6	0.713	12.30	3.86
		7	0.749	14.60	4.10
		8	0.865	18.05	4.24
	0.063 SF_6 -Ar	4	0.840	2.52	1.35
		5	0.935	4.82	1.86
		6	1.010	7.70	2.30

TABLE II
Gasdynamic Data (Cont.)

Nozzle	Gas	P_o Bar	P_1 Torr	P_{02} Torr	M_R
		7	1.095	10.57	2.61
		8	1.170	13.45	2.86
6	Ar	2	0.939	33.0	4.86
		3	1.093	44.5	5.23
		4	1.215	55.28	5.53
		5	1.326	59.59	5.50
		6	1.422	65.34	5.56
		7	1.501	71.09	5.65
	SF_6	2	0.694	22.21	5.19
		3	0.789	31.56	5.76
		4	0.900	38.75	5.97
		5	1.025	45.21	6.03
		6	1.146	50.25	6.02
		7	1.211	56.00	6.17
	0.03 SF_6 -Ar	2	0.637	22.21	4.95
		3	1.095	44.50	5.35
		4	1.187	54.56	5.70
		5	1.277	61.75	5.84
		6	1.352	68.93	6.00
		7	1.487	73.96	5.93
	0.0625 SF_6-Ar	2	0.932	16.46	3.57
		3	1.115	37.31	4.95
		4	1.229	55.28	5.75
		5	1.382	63.18	5.79
		6	1.433	71.09	6.04
		7	1.525	79.0	6.17
	0.125 SF_6 -Ar	2	0.925	18.62	3.93
		3	1.120	28.68	4.44

TABLE II
Gasdynamic Data (Cont.)

Nozzle	Gas	P_o Bar	P_1 Torr	P_{02} Torr	M_R
		4	1.275	38.75	4.84
		5	1.410	48.81	5.17
		6	1.475	56.0	5.42
		7	1.608	63.18	5.52
	He	2	1.581	5.68	1.45
		3	2.115	10.0	1.70
		4	2.376	21.50	2.41
		5	2.527	47.37	3.52
		6	2.666	90.50	4.77
		7	2.775	127.87	5.57
	0.125 SF_6 -He	2	1.190	7.12	2.07
		3	1.458	27.25	3.78
		4	1.739	45.93	4.51
		5	1.990	55.28	4.63
		6	2.130	61.75	4.73
		7	2.314	67.50	4.74
7	Ar	2	1.401	36.40	4.16
		3	1.753	76.12	5.40
		4	1.873	80.43	5.37
		5	2.083	87.62	5.32
		6	2.288	102.0	5.48
		7	2.490	109.18	5.43
	0.125 SF_6 -He	3	2.344	18.62	2.42
		4	2.834	33.71	2.99
		5	3.272	69.65	4.04
		6	3.681	119.25	5.00
	0.03 SF_6 -Ar	2	1.433	27.25	3.64
		3	1.701	64.62	5.17

TABLE II
Gasdynamic Data (Cont.)

Nozzle	Gas	P_o Bar	P_1 Torr	P_{02} Torr	M_R
		4	1.947	80.43	5.40
		5	2.169	89.06	5.38
		6	2.365	96.25	5.36
		7	2.572	105.59	5.38
		8	2.764	113.30	5.38
	0.063 SF_6 -Ar	2	1.402	25.09	3.59
		3	1.751	51.68	4.64
		4	2.003	73.25	5.17
		5	2.231	89.06	5.41
		6	2.423	102.00	5.56
		7	2.658	112.06	5.56
	SF_6	2	1.106	27.96	4.65
		3	1.41	39.46	4.88
		4	1.728	48.09	4.56
		5	2.066	56.0	4.80
		6	2.437	64.62	4.75
		7	2.868	71.09	4.60
		8	3.220	79.0	4.58
	Xe	4	3.641	20.06	1.85
		5	4.000	44.5	2.69
		6	4.245	90.5	3.77
		7	4.467	162.37	4.94
	0.125 SF_6 -Ar	2	1.409	24.37	3.63
		3	1.790	37.31	3.99
		4	2.099	44.5	4.03
		5	2.427	54.56	4.15
		6	2.693	66.06	4.34

TABLE III
COMPUTER SOLUTIONS FOR NOZZLE 7-B, 3% SF_6-Ar

Run No.	P_o Bar	Δ	F μ	$x^{\dagger}$ μ	P_1 Torr	P_{02} Torr	M
1	1	0.6	0.0006	0.88	1.03	20.4	3.64
2	1	0.6	0.0008	0.88	1.15	20.2	3.44
3	2.2	0.6	0.0002	0.37	1.46	n.c.	4.62
4	2.5	0.58	0.0002	0.37	1.63	46.7	4.39
5	3	0.6	0.0001	0.37	1.57	60.9	5.10
	3.5	0.6	0.0001	0.37	1.72	71.2	5.28
7	4	0.6	0.0001	0.37	1.88	n.c.	5.40
8	5	0.6	0.0001	0.37	2.21	n.c.	5.58
9	6	0.55	0.0003	0.37	2.16	98.3	5.19
10	7	0.52	0.0004	0.37	2.57	101.8	5.16
11	8	0.52	0.0004	0.37	2.78	116.6	5.31

n.c. - not calculated.

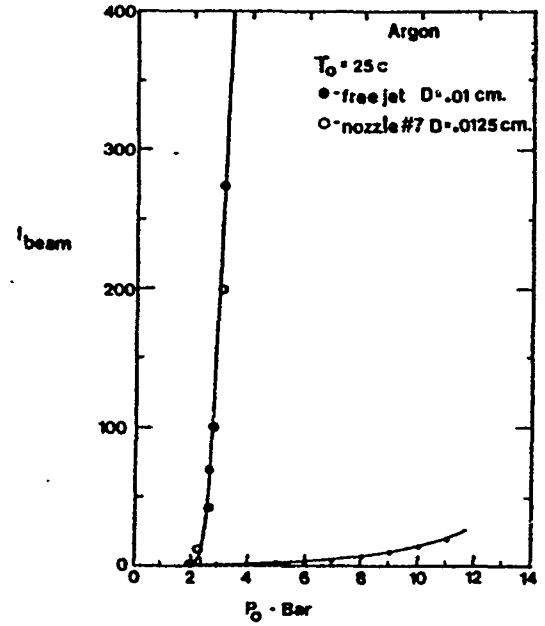

FIG. 1 Nozzle 7 is compared to a free jet source in a molecular beam configuration. The relative beam intensity I_B, primarily measures cluster intensity and shows the enormous advantage of the nozzle over the free jet. (Values of I_B greater than 100 are intense enough for experimental use.)

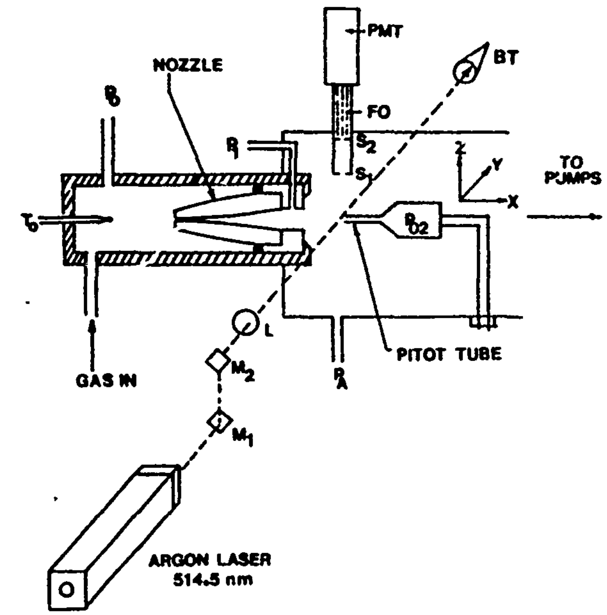

FIG. 2 The experimental arrangement permits nozzles and exit sections to be interchanged. Light scattering is used to detect condensation, M - mirror, L - lens, S - slit, FO - fiber optic, PMT - photomultiplier and BT - beam trap. The Pitot probe has x-y-z motion capability.

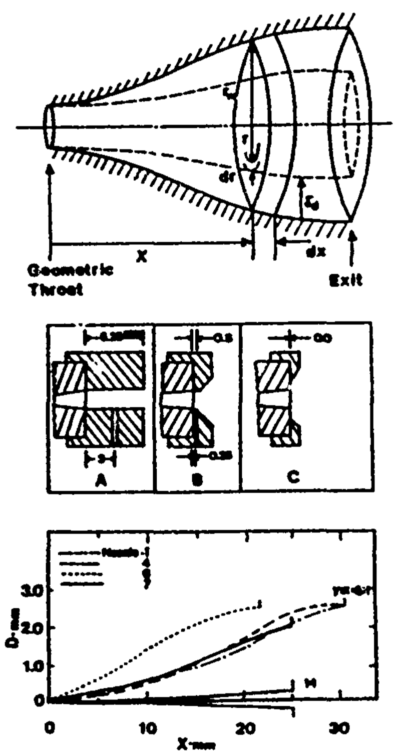

FIG. 3 The four glass nozzles discussed in this paper are shown expanded 8:1 in diameter in order to see the qualitative differences. A 1:1 contour of Nozzle 7 shows the actual geometry. Three exit sections A, B, and C were attached to the nozzles to test the effect of nozzle length and to provide a static pressure tap in the case of exit sections A and B (See Table I for additional details). The upper part of the figure shows the coordinates for the solution to the equations of motion, plus the boundary layer displacement thickness.

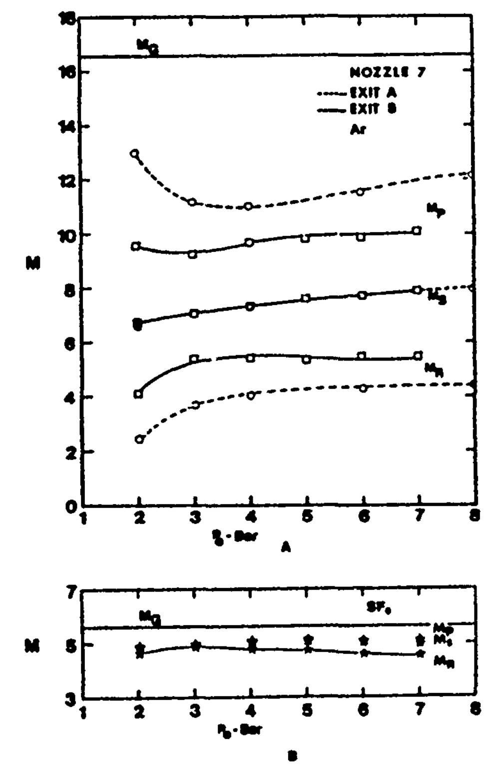

FIG. 4 The exit Mach number for Nozzle 7 is plotted as dashed lines for exit A and solid lines for exit B. The Mach number M_s is based on the static pressure measurement, Eqn. (4), M_p is based on the Pitot measurements and Eqn. (5), and M_R is based on both measurements at the exit and Eqn. (6). The geometric Mach number M_G is based on area ratio only, i.e. no viscous effects, and is the upper limit. The correct Mach number is M_R and the deviation from the other Mach numbers is due to viscous effects. Note the closeness of the three Mach numbers in the case of SF_6 indicating little or no viscous dissipation in the "isentropic" core. The data provide increasing Mach numbers in the order M_R, M_s, and M_p at any given p_0 although the symbols overlap for the SF_6 case.

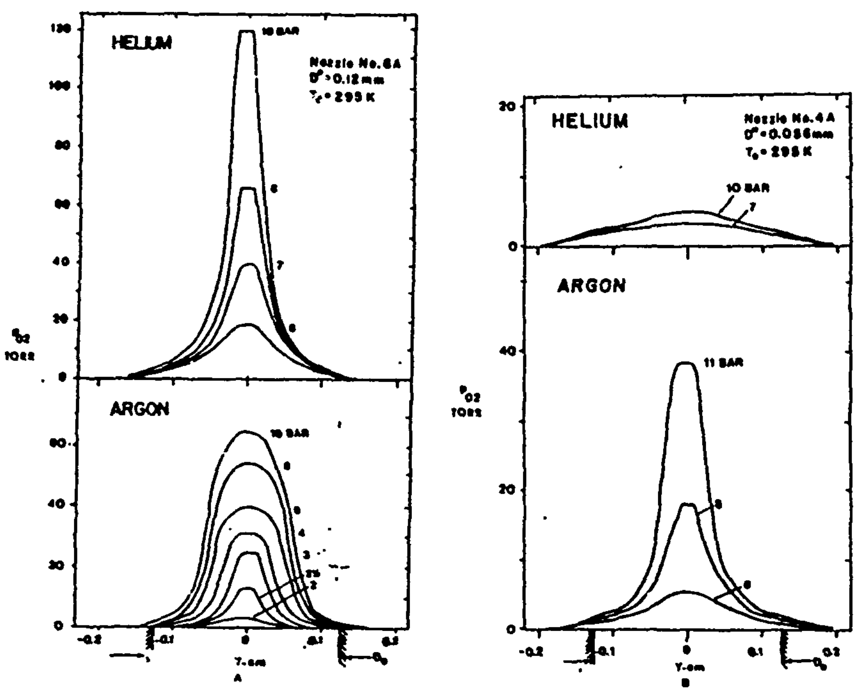

FIG. 5 Pitot traverses, for varying stagnation pressure, are shown for Nozzle 6 (relatively large throat size) and Nozzle 4 (small throat size) for helium and argon flows both using exit configuration A shown in Fig. 1. A larger diameter nozzle provides more intense beams or higher exit Mach numbers. Nozzle 4 is virtually of no use with helium. (The nozzle exit diameter is D_e.)

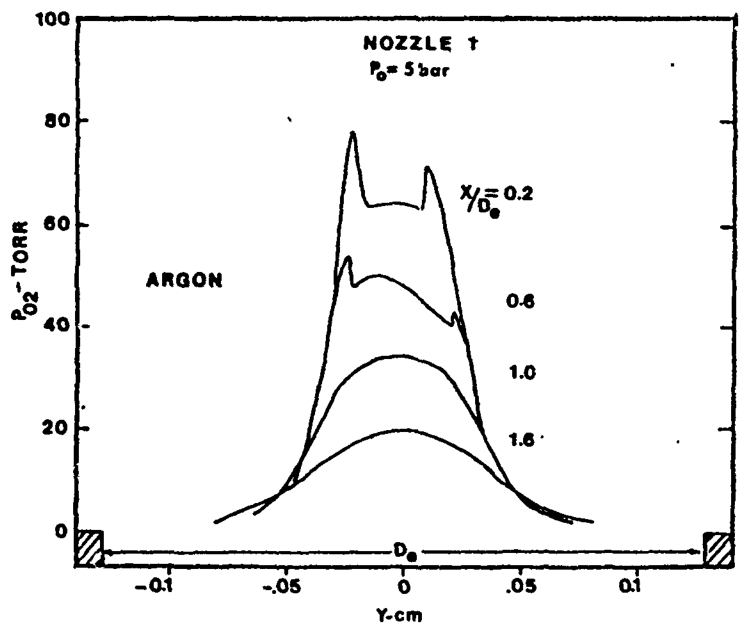

FIG. 6 Pitot traverses across the *flow beyond the exit of Nozzle 1*, Exit B, for argon are shown as a function of position downstream of the exit. Note the flat core section close to the nozzle exit which disappears progressively downstream. Here x is measured from 0.5 mm beyond the exit plane of the glass nozzle.

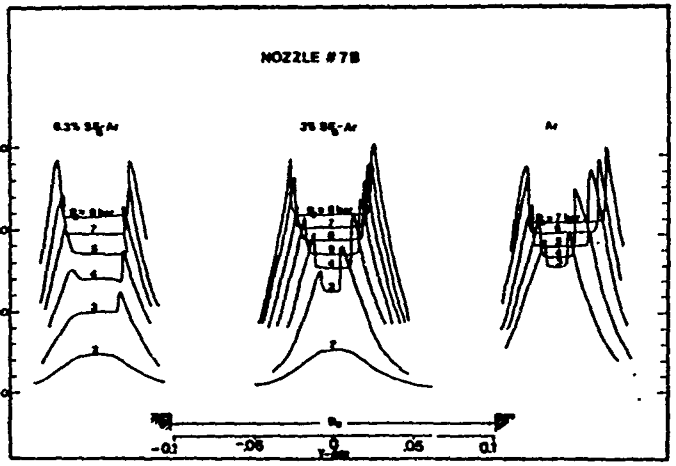

FIG. 7 Pitot profiles for Nozzle 7-B as a function of p_0 are shown for argon, 3% and 6.3% SF_6 in argon. For one gas the decrease in the core size with decreasing pressure is due to progressively thicker boundary layers, i.e. lower Reynolds numbers. The variation in core size and centerline Pitot pressure from one mixture to another is due to a combination of variation in γ and δ. The measurements were made in the exit plane of the glass nozzle (i.e., x/D_e = -0.25 in Fig. 6).

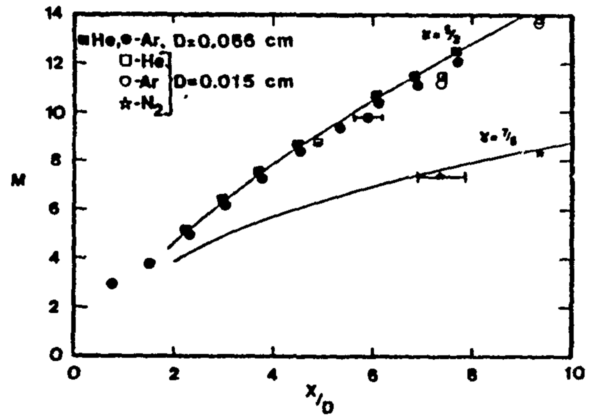

FIG. 8 Pitot measurements are shown for two free jets with a factor of 25 difference in throat area and several gases. Mach number from Eqn. (5) is compared to the theoretical values given by Eqn. (7). This theory has been verified with numerous types of measurements and is applicable for the x/D > 2.

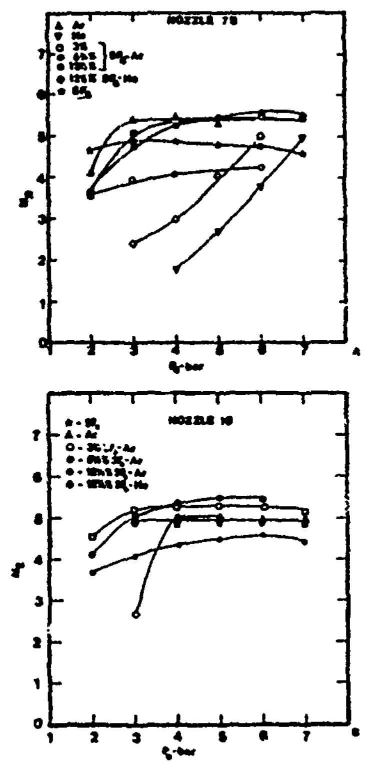

FIG. 9 Mach numbers are plotted with properties based on the initial mole fractions for mixtures and are nearly independent of P_o above 3 bar, except for He and He-SF_6, while SF_6 is constant over the entire range. Nozzle 1 shows a slightly larger variation in exit Mach numbers for the Ar and Ar-SF_6 mixtures. The He-SF_6 mixture turns over toward a flat value in this nozzle but the pure helium does not.

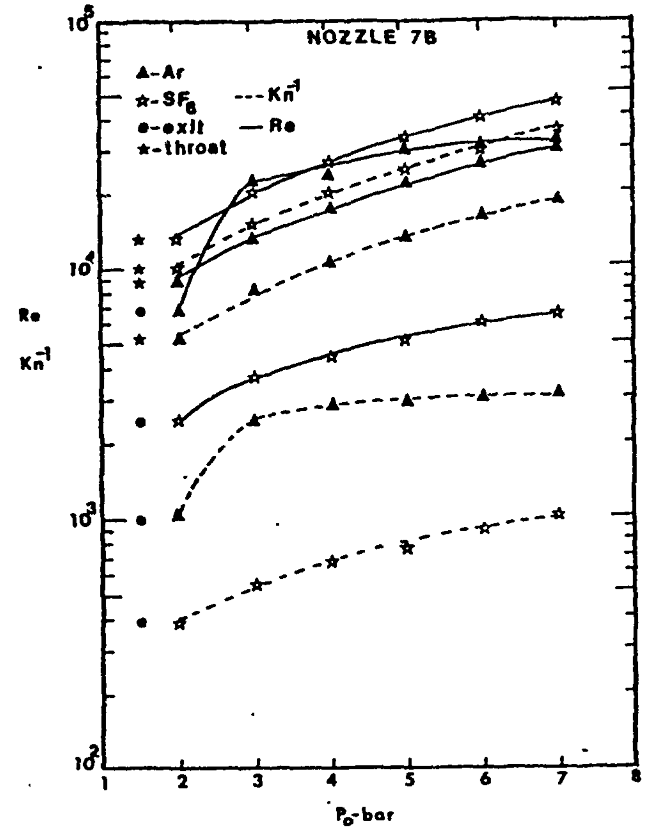

FIG. 10 Typical values of Reynolds number Re and inverse Knudsen number Kn^{-1} for Ar and SF_6 in Nozzle 7 are shown with * - the throat properties and e - the exit. The characteristic dimension for both parameters is the nozzle diameter and shows that the flows are still collision dominated even at the lower pressures. A wider variation exists for He.

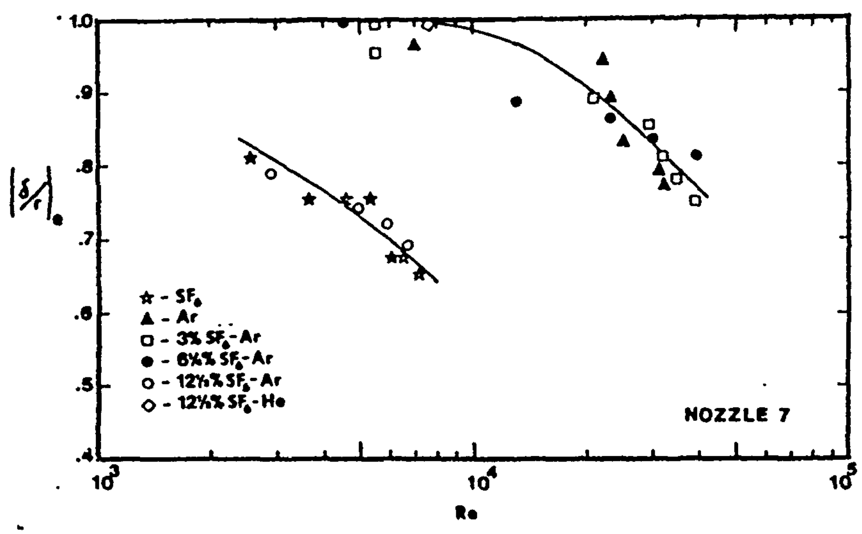

FIG. 11 The exit boundary layer thickness, δ, divided by nozzle radius r is plotted as a function of exit Reynolds number. Pitot traverses provide δ using exit B or C. The upper limit of $(\delta/r)_e$ = 1.0 represents a fully developed flow. The lower curve is the displacement thickness $(\delta_d/r)_e$ obtained from M_R.

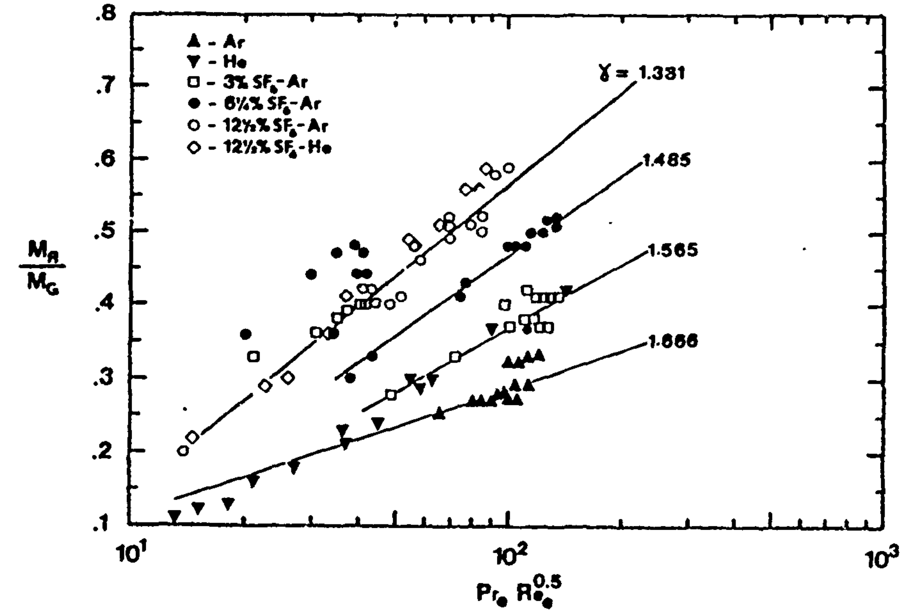

FIG. 12 The ratio M_R/M_G is an indication of the boundary layer displacement thickness and is shown as a function of $Re^{.5}$ Pr.

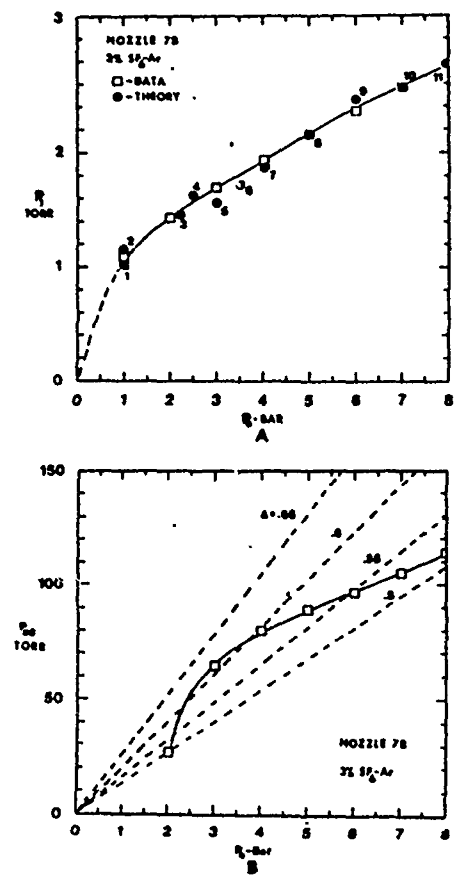

FIG. 13 The static and the Pitot pressure data for 3% SF_6-Ar in Nozzle 7 are compared with theoretical solutions shown as solid lines.

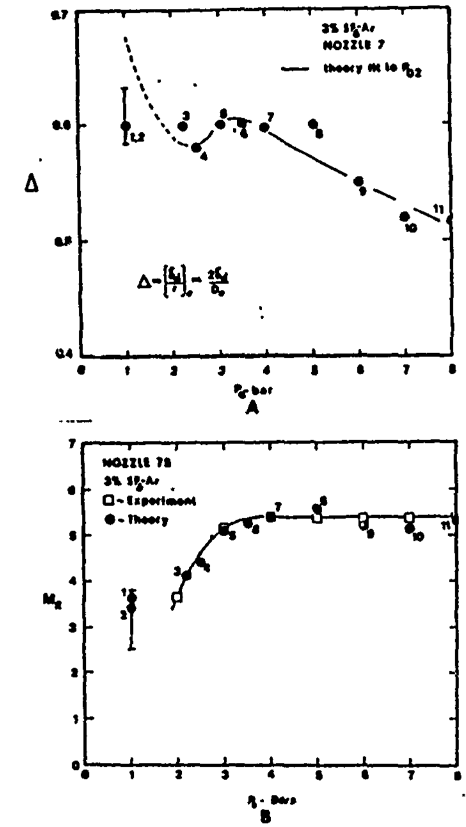

FIG. 14 The parameters for the theoretical solutions of Fig. 14 are shown in part A. Part B compares the exit Mach number from the computer calculations, that include the variation of properties with temperature and condensation, to that obtained from the data and one-dimensional gasdynamics using isentropic exit properties and no phase change.